Supplementary Information for

Heterogeneous synthesis of perovskite quantum dots for efficient blue LEDs

Jie Chen[1,2,†], Wanying Zhang[1,†], Xinyang Zhang[1,†], Yingwei Wang[3], Zhuoyin Peng[4], Fan Xia[1,5,*], Keqiang Chen[1,2,*], Guogang Li[1,2,*]

[1]Faculty of Materials Science and Chemistry, China University of Geosciences, Wuhan 430074, P. R. China

[2]Shenzhen Research Institute, China University of Geosciences, Shenzhen 518052, P. R. China

[3]Hunan Key Laboratory of Nanophotonics and Devices, School of Physics and Electronics, Central South University, Changsha 410083, P. R. China

[4]College of Energy and Power Engineering, Changsha University of Science and Technology, Changsha 410114, P. R. China

[5]State key Laboratory of Biogeology and Environmental Geology, China University of Geosciences, 388 Lumo Road, Wuhan 430074, P. R. China

[†]These authors contributed equally: Jie Chen, Wanying Zhang, Xinyang Zhang.

Correspondent:

[*] Prof. Fan Xia

E-mail: xiafan@cug.edu.cn

Prof. Keqiang Chen

E-mail: chenkeqiang@cug.edu.cn

Prof. Guogang Li

E-mail: ggli@cug.edu.cn

Table of Contents:

I. Supplementary figures

Supplementary Fig. 1. Monitoring the synthesis of $CsPbBr_xCl_{3-x}$ QDs.

Supplementary Fig. 2. Dissolution behaviour of lead halides.

Supplementary Fig. 3. Effect of DBSA on lead halide dissolution behaviour.

Supplementary Fig. 4. Thermodynamic role of lead halide precipitate.

Supplementary Fig. 5. Formation mechanism of $CsPbBr_xCl_{3-x}$ QDs.

Supplementary Fig. 6. Characterization of homo-QDs.

Supplementary Fig. 7. Characterization of hetero-QDs.

Supplementary Fig. 8. Compositional analysis by XPS depth profiling.

Supplementary Fig. 9. Electronic properties.

Supplementary Fig. 10. TA spectroscopy.

Supplementary Fig. 11. PL stability.

Supplementary Fig. 12. Thermal stability.

Supplementary Fig. 13. Exciton binding energy characterization.

Supplementary Fig. 14. TOAF passivation.

Supplementary Fig. 15. Characterization of hetero-TOAF-QDs.

Supplementary Fig. 16. XPS characterization.

Supplementary Fig. 17. Temperature-dependent emission behaviour.

Supplementary Fig. 18. Characterization of TOAF-passivated hetero-QDs.

Supplementary Fig. 19. UPS measurement.

Supplementary Fig. 20. EL performance.

Supplementary Fig. 21. The third-party test report.

Supplementary Fig. 22. Operation stability.

Supplementary Fig. 23. Transient photocurrent responses.

Supplementary Fig. 24. Determination of ion migration activation energy.

Supplementary Fig. 25. Ion migration.

Supplementary Fig. 26. Stability characterization of LEDs.

Supplementary Fig. 27. LED performance.

Supplementary Fig. 28. Blue LEDs with different emission wavelengths.

Supplementary Fig. 29. Colour purity of the tunable blue LEDs.

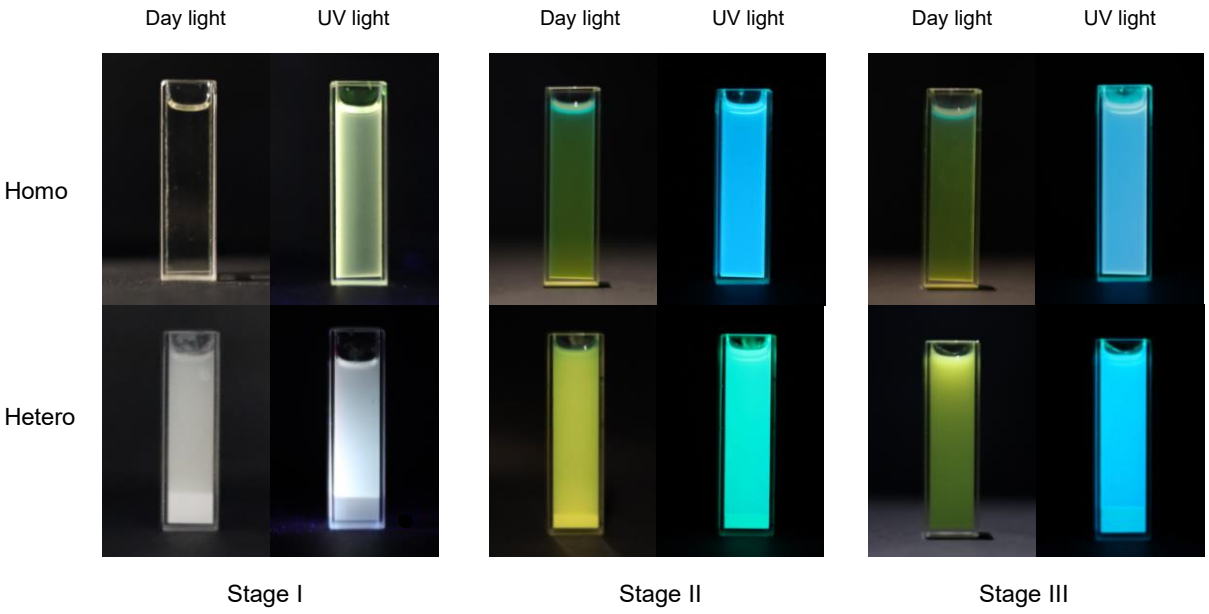
II. Supplementary tables

Supplementary Table 1. Precursor feeding amounts for the synthesis of QDs with tunable PL peaks.

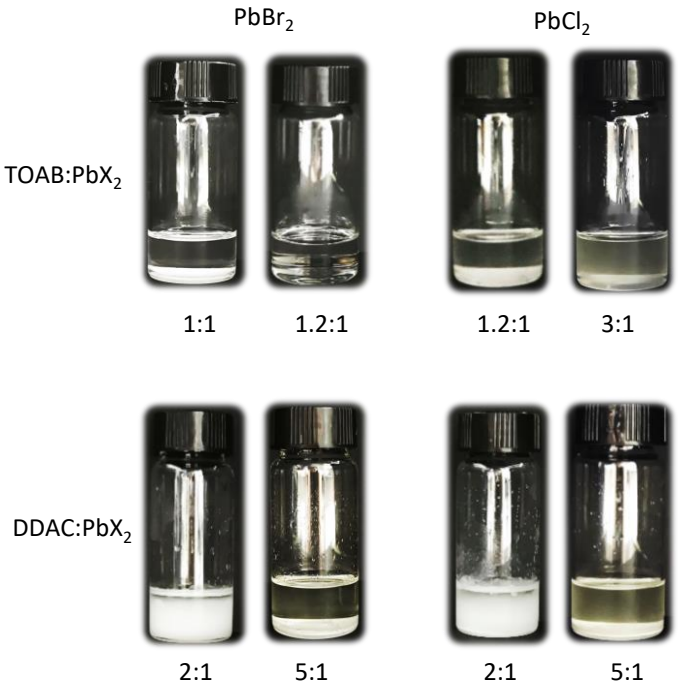
Supplementary Table 2. Wavelength-dependent PLQYs of the different QDs.

Supplementary Table 3. Summarized device data of recently reported blue perovskite LEDs.

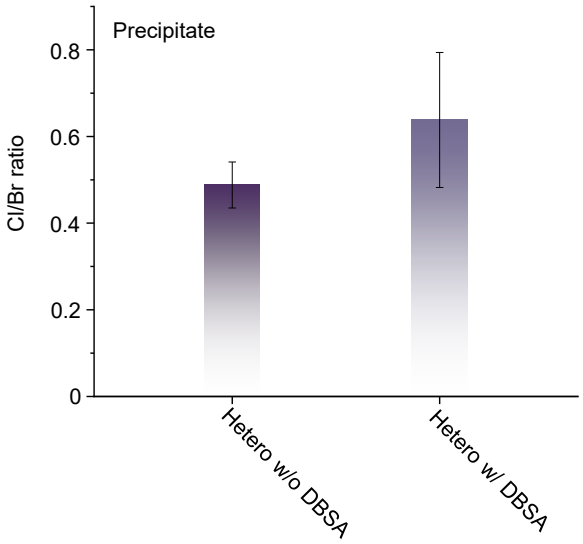
III. Supplementary references



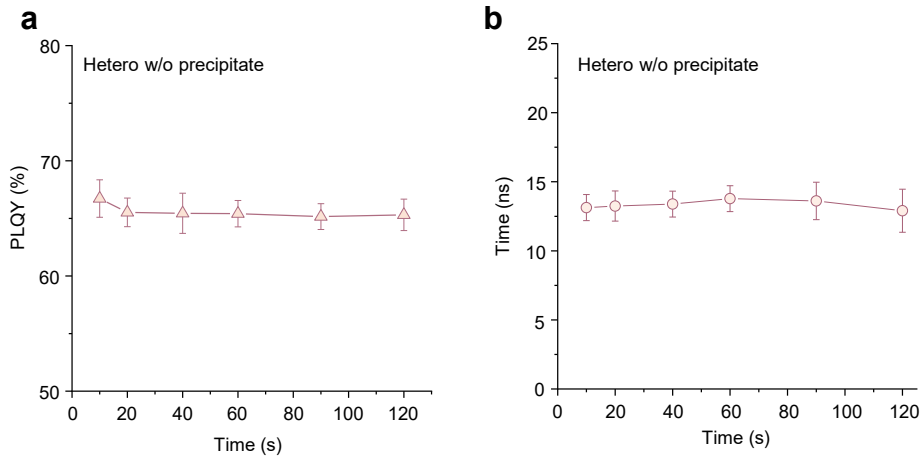
Supplementary Fig. 1. Monitoring the synthesis of $CsPbBr_xCl_{3-x}$ QDs. Optical photographs of the reaction mixtures taken under daylight and UV illumination at different stages corresponding to **Fig. 1a**. In contrast to the persistently clear homogeneous solution, the heterogeneous system contains a conspicuous solid precipitate throughout the reaction.



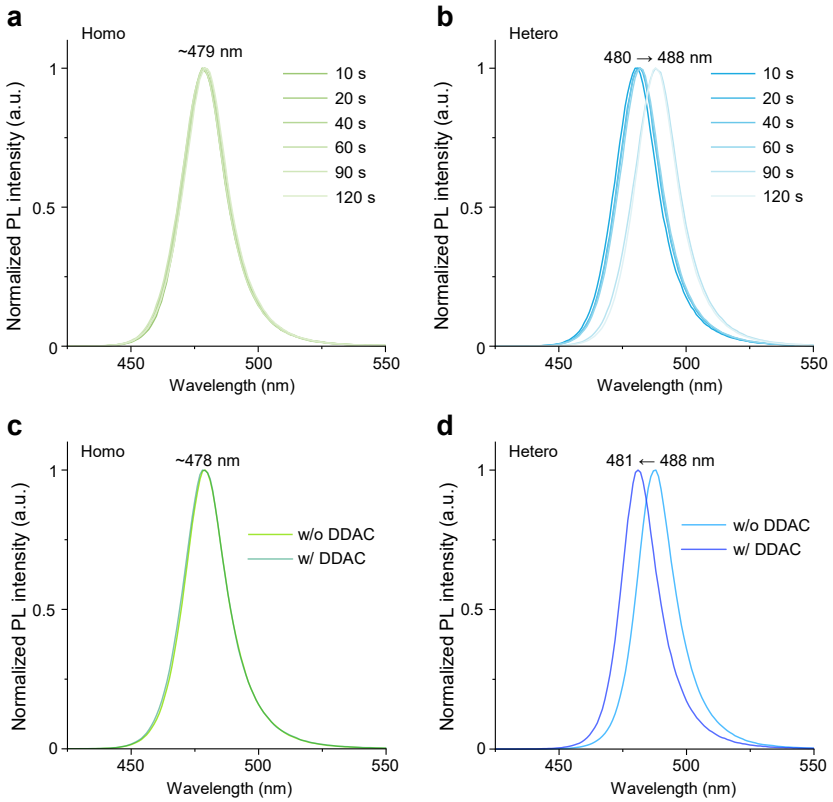
Supplementary Fig. 2. Dissolution behaviour of lead halides. Optical photographs of lead halides in TOAB or DDAC at various molar ratios. Complete dissolution of $PbBr_2$ is achieved at a TOAB:$PbBr_2$ ratio of 1.2, whereas $PbCl_2$ remains insoluble even at a threefold excess of TOAB. DDAC shows markedly inferior dissolving capability, with incomplete dissolution of both halides persisting up to a fivefold excess.



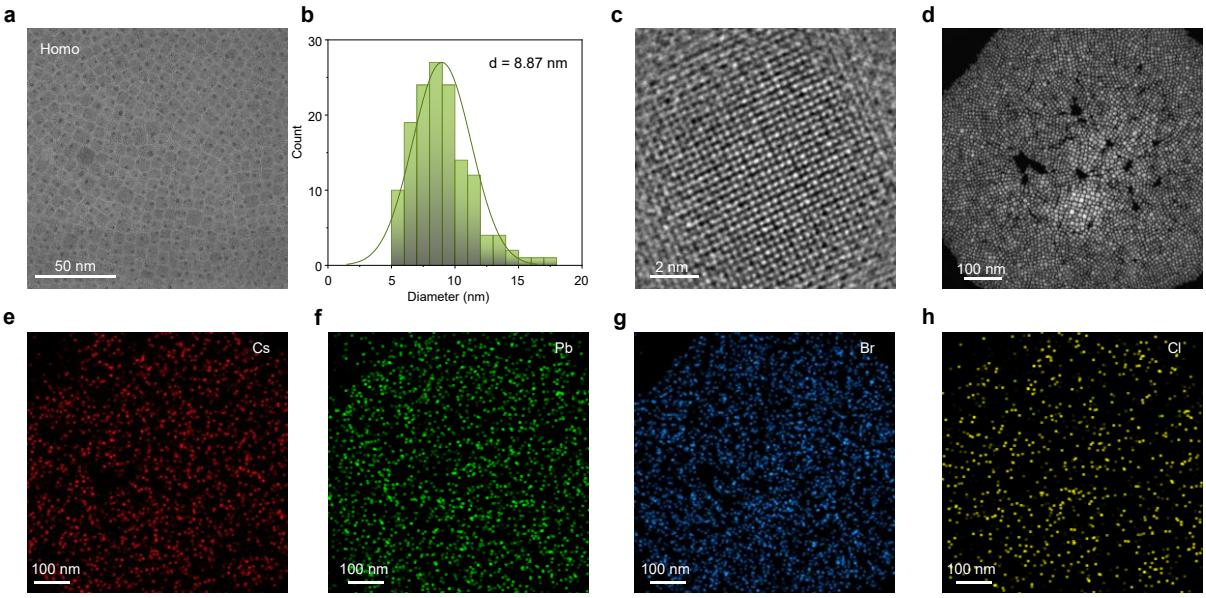
Supplementary Fig. 3. Effect of DBSA on lead halide dissolution behaviour. Cl/Br ratios in the precipitate of the heterogeneous system measured before and after DBSA addition. Precipitates were isolated by centrifugation and dried before analysis. The increase in the Cl/Br ratio after DBSA addition further confirms the preferential depletion of Cl^-.



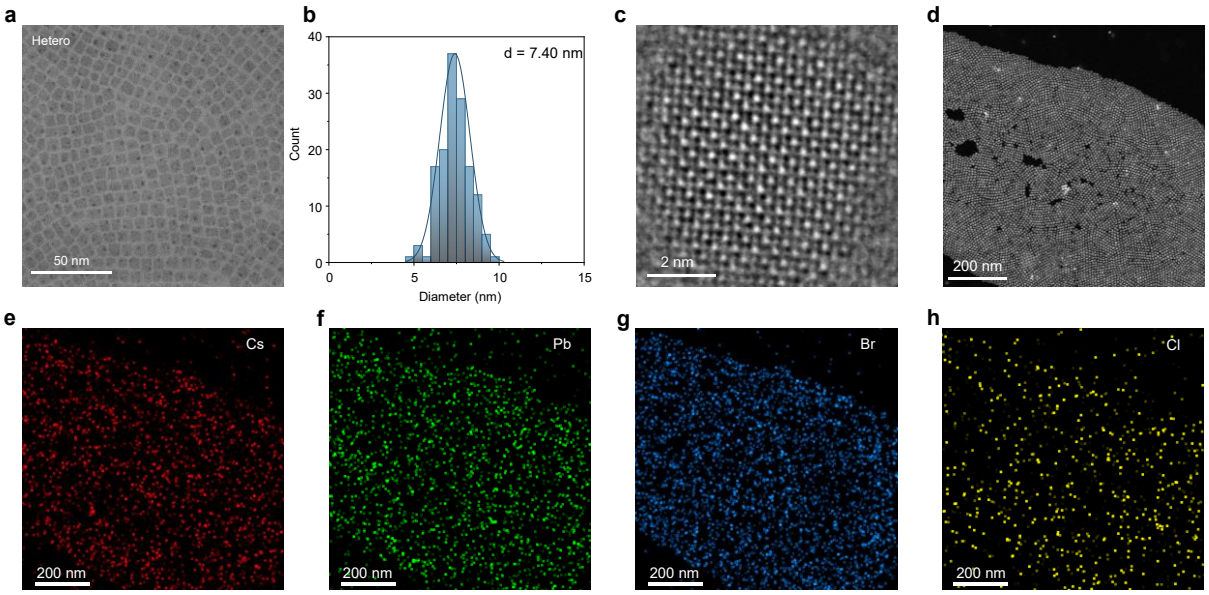
Supplementary Fig. 4. Thermodynamic role of lead halide precipitate. a,b, Time-dependent PLQY (**a**) and PL lifetime (**b**) of QDs after Cs-precursor injection in the heterogeneous system from which the lead halide precipitate had been removed prior to the reaction. Compared with the results in **Fig. 1c**, the enhancements observed previously are completely eliminated, confirming the essential role of the lead halide solid phase.



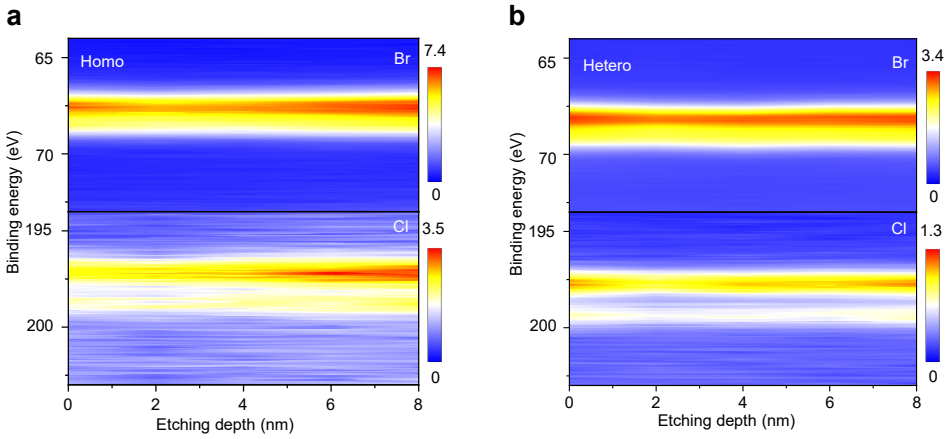
Supplementary Fig. 5. Formation mechanism of $CsPbBr_xCl_{3-x}$ QDs. a,b, Time-dependent PL spectra of the homo-QDs (**a**) and hetero-QDs (**b**) following Cs-precursor injection. **c,d**, The effect of DDAC on the PL spectra of homo-QDs (**c**) and hetero-QDs (**d**).



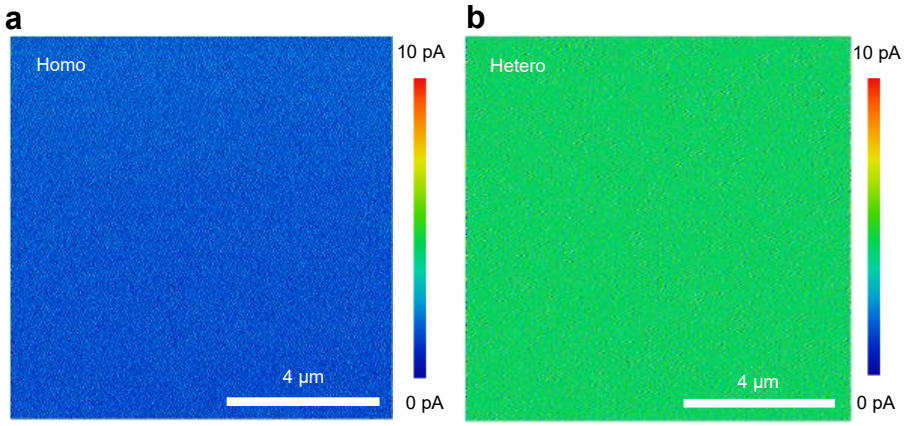
Supplementary Fig. 6. Characterization of homo-QDs. a,b, TEM image (**a**) and corresponding size histogram (**b**). **c**, HRTEM image. **d**, HAADF-STEM image. **e-h**, TEM-EDS elemental mapping of Cs (**e**), Pb (**f**), Br (**g**), and Cl (**h**).



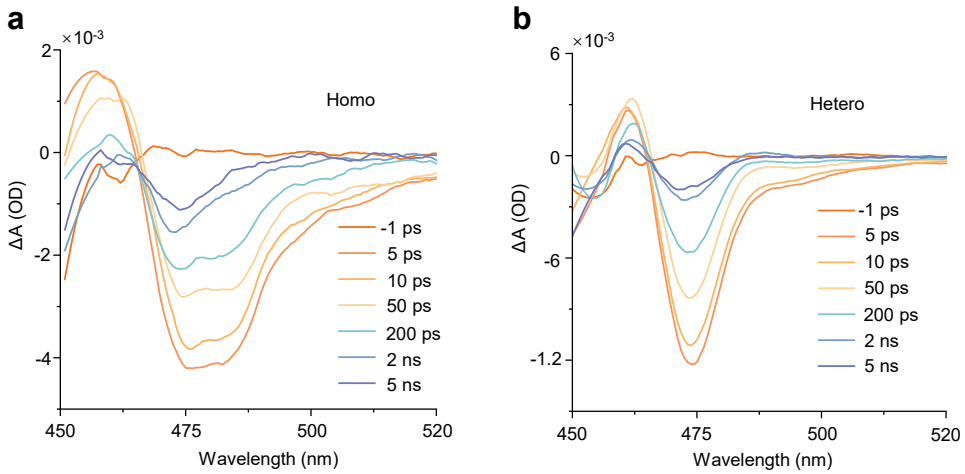
Supplementary Fig. 7. Characterization of hetero-QDs. a,b, TEM image (**a**) and corresponding size histogram (**b**). **c**, HRTEM image. **d**, HAADF-STEM image. **e-h**, TEM-EDS elemental mapping of Cs (**e**), Pb (**f**), Br (**g**), and Cl (**h**). The average size of hetero-QDs (7.40 nm) is markedly smaller than that of homo-QDs (8.87 nm). We attribute this to the role of undissolved lead halides as heterogeneous nucleation sites, which consume a large fraction of the monomers and thereby reduce the monomer supply available for subsequent QD growth, ultimately restricting particle growth and leading to the observed smaller size.



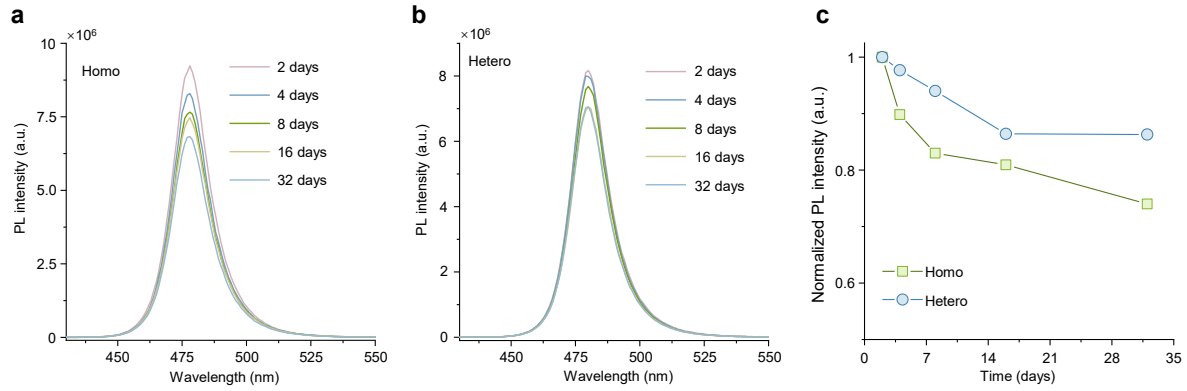
Supplementary Fig. 8. Compositional analysis by XPS depth profiling. a,b, High-resolution XPS spectra acquired at various etching depths for homo-QDs (**a**) and hetero-QDs (**b**).



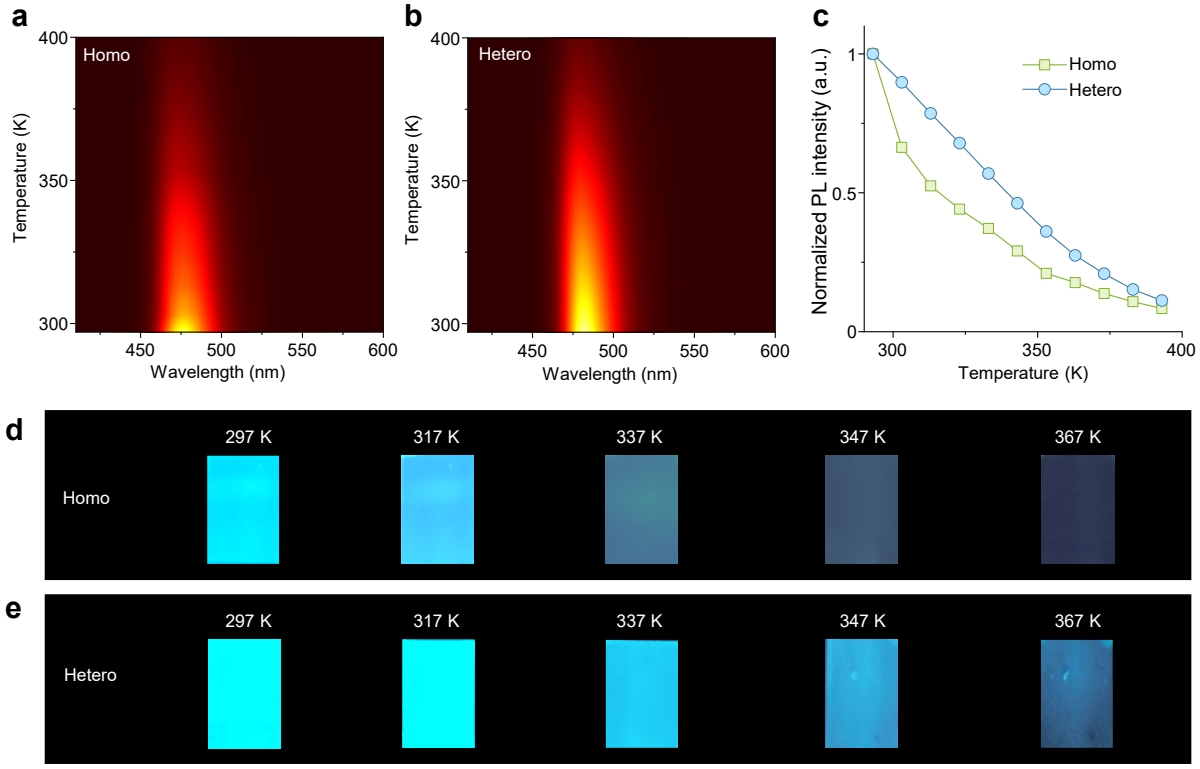
Supplementary Fig. 9. Electronic properties. a,b, CAFM images of homo-QDs (**a**) and hetero-QDs (**b**).



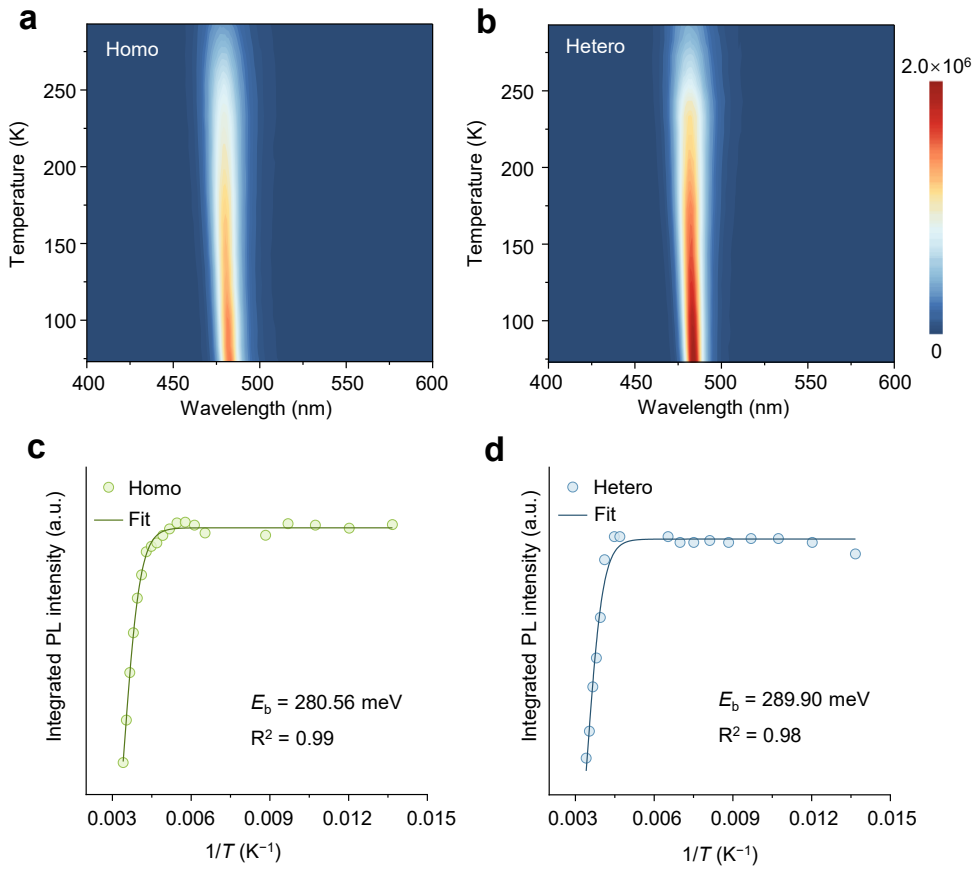
Supplementary Fig. 10. TA spectroscopy. a,b, Principal component spectra obtained from TA measurements for homo-QDs (**a**) and hetero-QDs (**b**) across a pump-probe delay window of −1 fs to 5 ns.



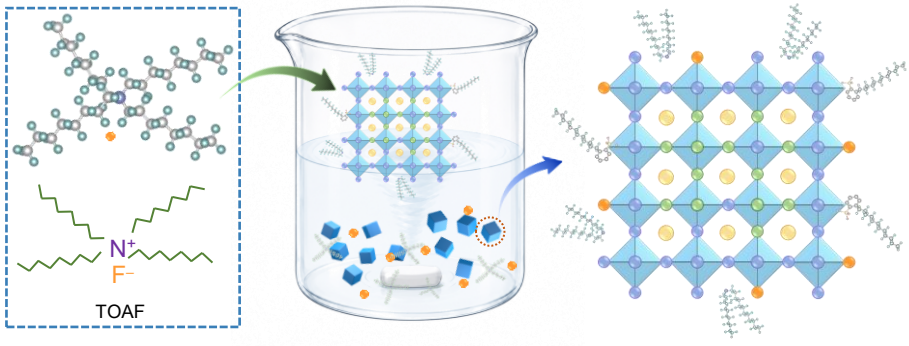
Supplementary Fig. 11. PL stability. a,b, PL spectra recorded at different aging times for homo-QDs (**a**) and hetero-QDs (**b**). **c**, Corresponding integrated PL intensity decay profiles.



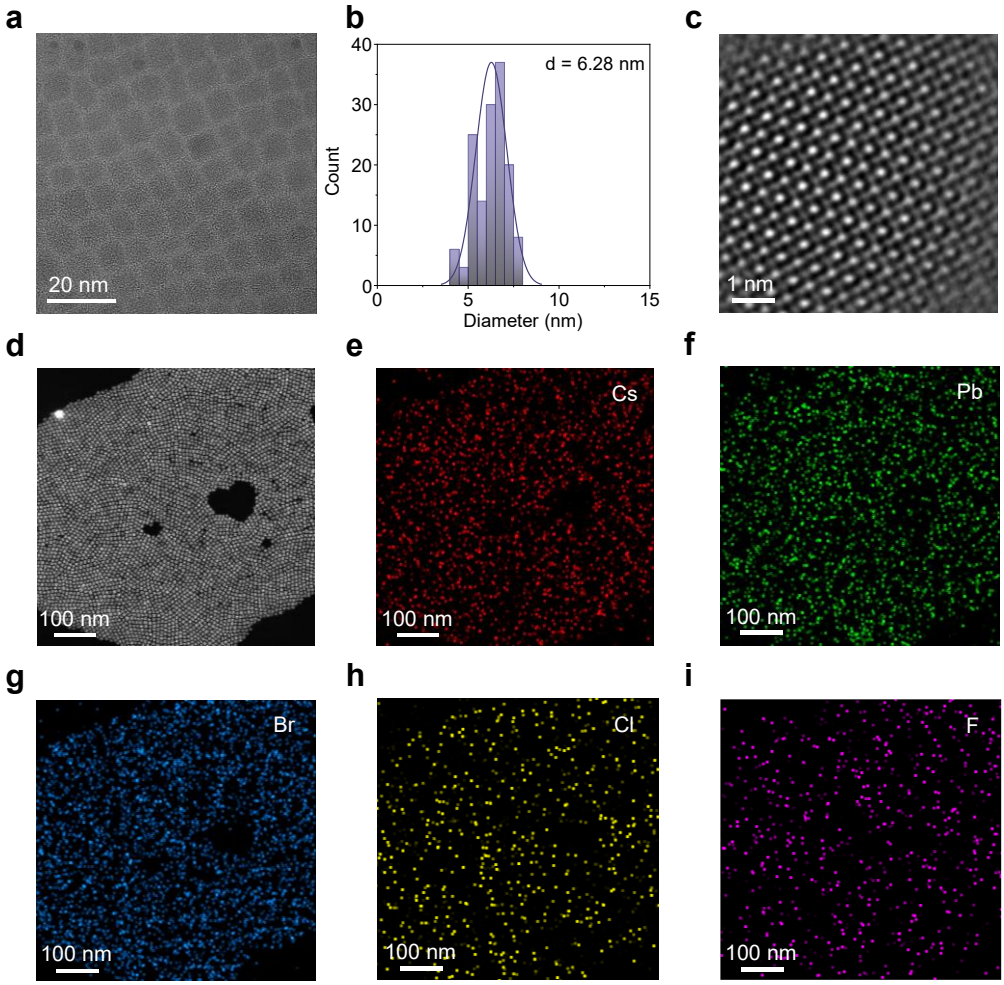
Supplementary Fig. 12. Thermal stability. a,b, Temperature-dependent PL intensity maps for homo-QDs (**a**) and hetero-QDs (**b**). **c**, Corresponding integrated PL intensity decay profiles. **d,e**, Photographs of homo-QD (**a**) and hetero-QD (**b**) films under UV irradiation at different temperatures.



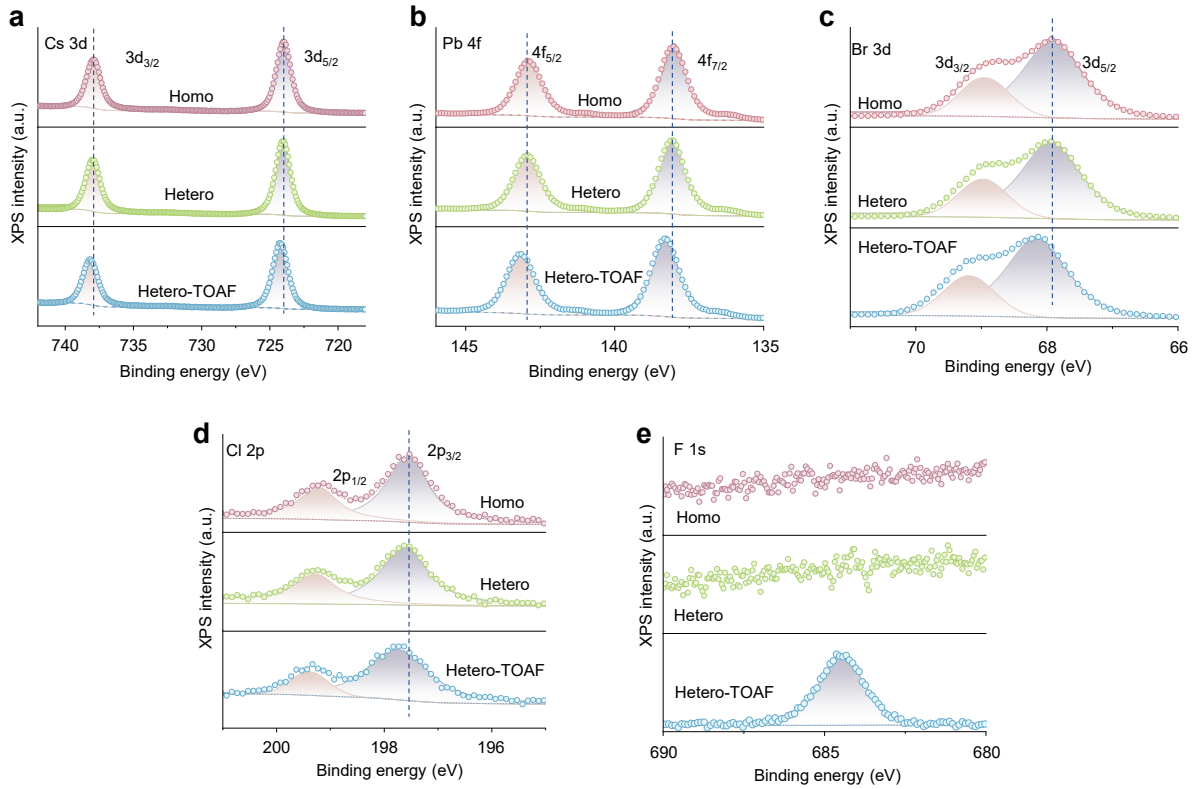
Supplementary Fig. 13. Exciton binding energy characterization. a,b, Temperature-dependent PL intensity maps for homo-QDs (**a**) and hetero-QDs (**b**). **c,d**, Corresponding integrated PL intensity intensities as a function of temperature for homo-QDs (**c**) and hetero-QDs (**d**).



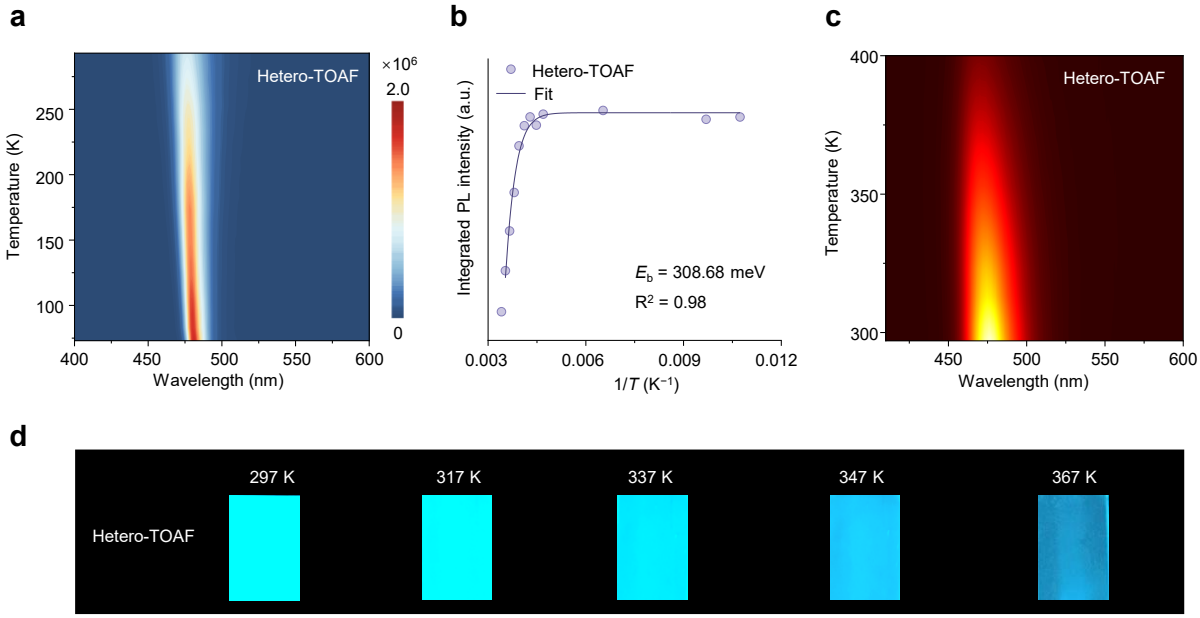
Supplementary Fig. 14. TOAF passivation. Schematic illustrations of TOAF passivation.



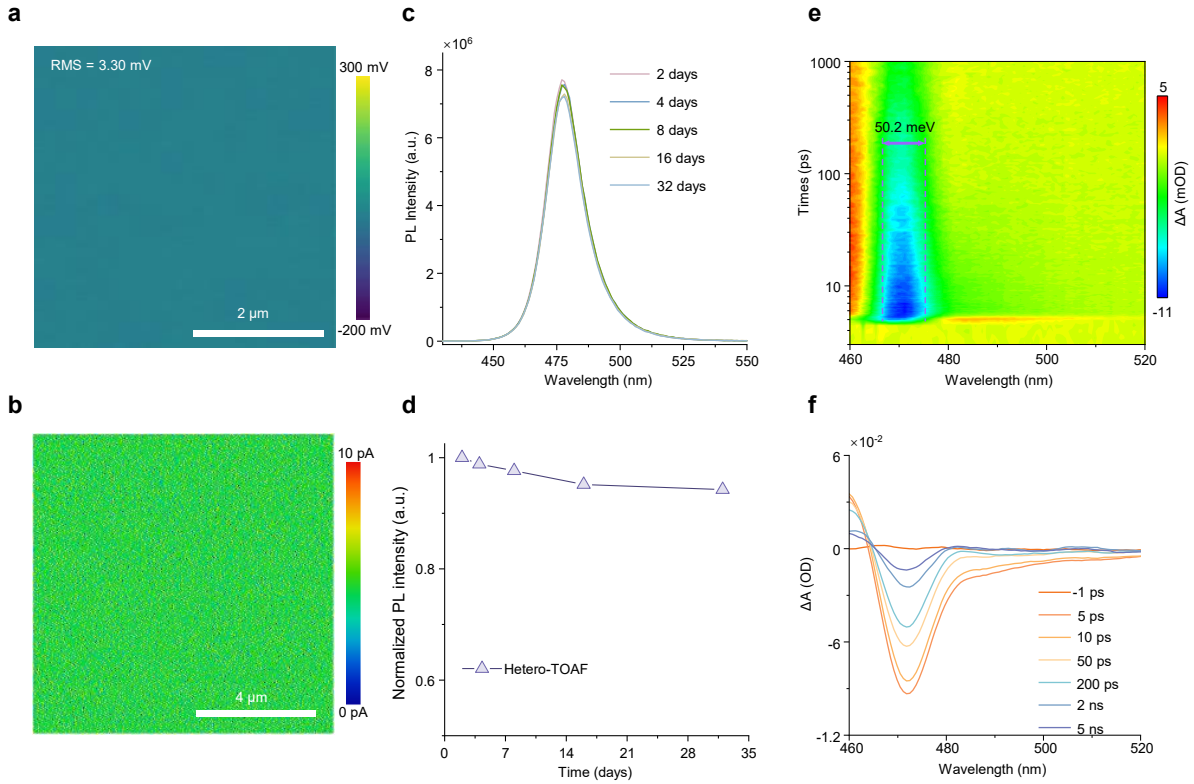
Supplementary Fig. 15. Characterization of hetero-TOAF-QDs. a,b, TEM image (**a**) and corresponding size histogram (**b**). **c**, HRTEM image. **d**, HAADF-STEM image. **e-i**, TEM-EDS elemental mapping of Cs (**e**), Pb (**f**), Br (**g**), Cl (**h**), and F (**i**).



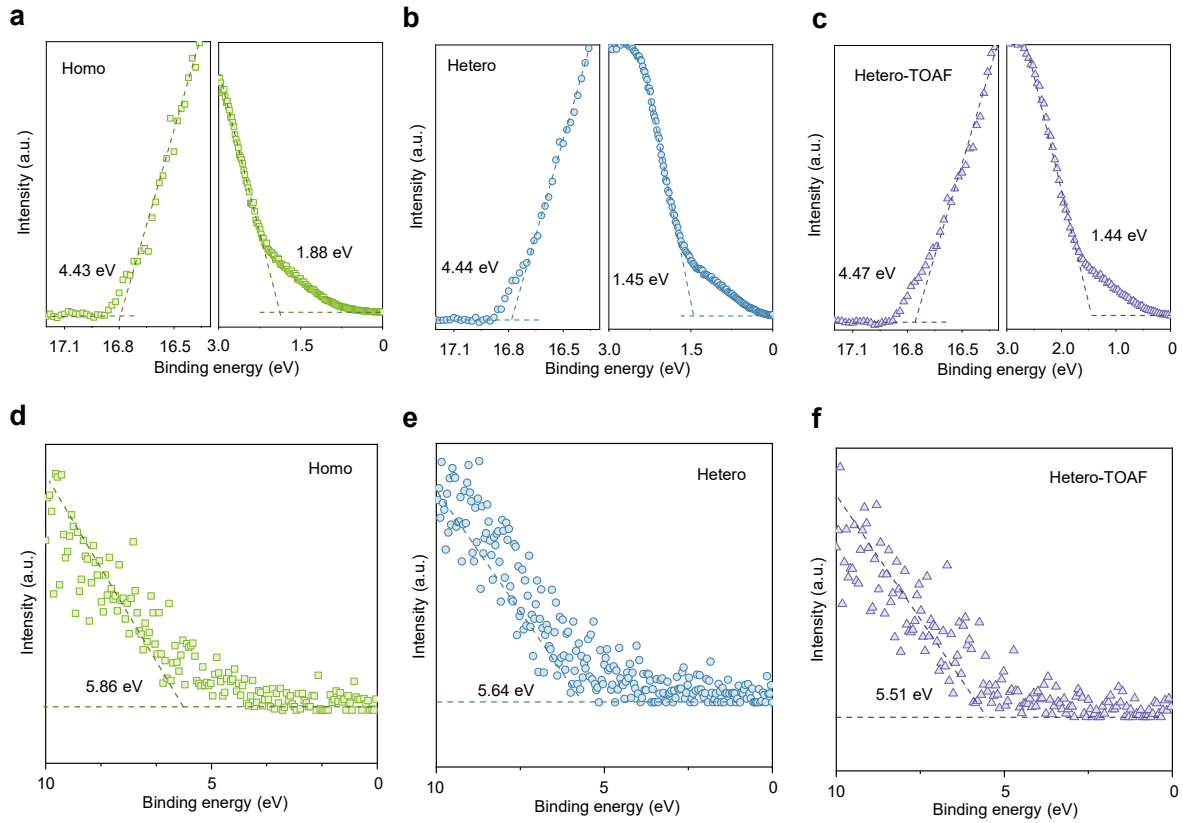
Supplementary Fig. 16. XPS characterization. a-e, High-resolution XPS spectra of Cs (**a**), Pb (**b**), Br (**c**), Cl (**d**), and F (**e**).



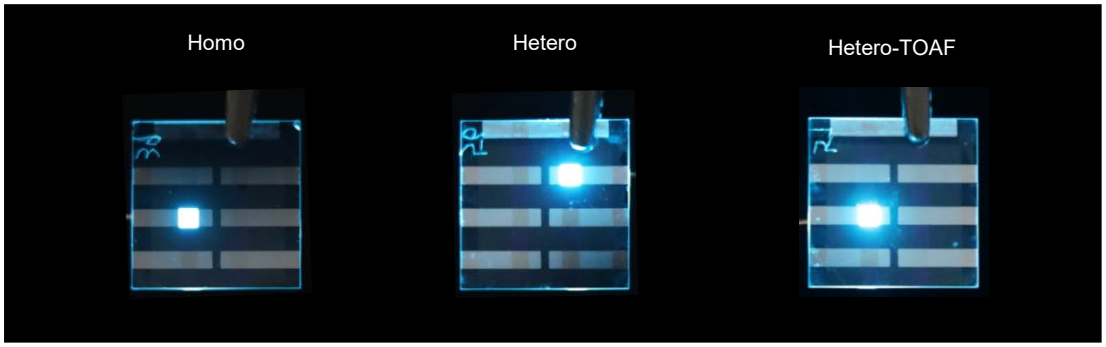
Supplementary Fig. 17. Temperature-dependent emission behaviour of hetero-TOAF-QDs. a,b, Low-temperature PL intensity map (**a**) and corresponding integrated intensity profile (**b**). **c**, High-temperature PL intensity map. **d**, Photographs of the QD film under UV irradiation at different temperatures.



Supplementary Fig. 18. Characterization of TOAF-passivated hetero-QDs. a, KPFM image. **b**, CAFM image. **c,d**, Evolution of PL spectra (**c**) and integrated intensity (**d**) upon aging. **e**, Pseudo-colour TA spectra and pump-detection delay time. **f**, principal spectra extracted at the time delay ranging from −1 fs to 5 ns.



Supplementary Fig. 19. UPS measurement. a-f, UPS spectra of homo-QDs (**a** and **d**), hetero-QD (**b** and **e**), and hetero-TOAF-QD (**c** and **f**) films.



Supplementary Fig. 20. EL performance. Optical photographs of operating devices.

№: WTS2026-A1093

检验报告
TEST REPORT

委托单位: Client:	:	中国地质大学（武汉） / China University of Geosciences (Wuhan)
委托单位地址: Client Address:	:	湖北省武汉市洪山区鲁磨路 388 号 / No. 388 Lumo Road, Wuhan, Hubei Province, China
产品名称 Product Name	:	钙钛矿量子点LED / Perovskite QD-based LED
型号规格 Model / Specification	:	Blue-476.329 nm
检测机构 Testing Body	:	浙江中协立德质量检测技术有限公司 Zhejiang Zhongxie Lide Quality Testing Technology Co., Ltd.
	:	浙江省宁波市慈溪市新浦镇横新路 321-323 号(市技术监督局新浦分所南) No. 321-323 Zhengxin Road, Xinpu Town, Cixi City, Ningbo, Zhejiang, China (south of Xinpu Branch, Cixi Municipal Bureau of Technical Supervision)
报告日期 Report Date	:	2026 年 11 月 2 日 / Nov. 2, 2026
检验类别 Test Category	:	委托检验 Commissioned Inspection

检验机构:浙江中协立德质量检测技术有限公司
Testing Body: Zhejiang Zhongxie Lide Quality Testing Technology Co., Ltd.

浙江中协立德质量检测技术有限公司
Zhejiang Zhongxie Lide Quality Testing Technology Co., Ltd.

№: WTS2026-A1093

检测结果汇总表格
SUMMARY OF TEST RESULT

序号 No.	检验项目 Test Item(s)	测试方法 Test Method	检验结果 Result	判定 Judgement
1	外量子效率与亮度 / External quantum efficiency and luminance	在氮气氛围手套箱内室温测试（有效发光面积 4mm²），使用 Keithley 2400 源表、积分球（Shenzhen Pynect）、QE Pro 光谱仪（Ocean Optics）及辐照度校准光源（HL-3P-INT-CAL, Ocean Optics）。Tested at room temperature in a nitrogen-filled glovebox (active area: 4 mm²) using a Keithley 2400 source meter, an integrating sphere (Shenzhen Pynect), a QE Pro spectrometer (Ocean Optics) and an irradiance calibration light source (HL-3P-INT-CAL, Ocean Optics).	输入电压 3.4 V；电流密度 0.689216 mA/cm²；最大外量子效率 36.96412%(对应亮度 180.14699 cd/m²)；峰值波长 476.329 nm。Input voltage: 3.4 V; current density: 0.689216 mA/cm²; maximum external quantum efficiency: 36.96412% (at a luminance of 180.14699 cd/m²); peak wavelength: 476.329 nm.	符合 / Compliant
2	电致发光光谱 / Electroluminescence spectra	在不同驱动电压下采集电致发光光谱并记录 V-J-L-EQE特性。Electroluminescence spectra were collected at various driving voltages, and the V-J-L-EQE characteristics were recorded.	各工作电压下的电致发光光谱及 V-J-L-EQE数据详见附件 I～V。The EL spectra and V-J-L-EQE data at each operating voltage are provided in Attachments I - V.	符合 / Compliant

浙江中协立德质量检测技术有限公司
Zhejiang Zhongxie Lide Quality Testing Technology Co., Ltd.

№: WTS2026-A1093

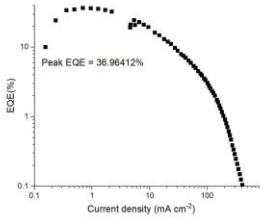
Attachment I

V (V)	J (mA/cm²)	L (cd/m²)	EQE (%)	V (V)	J (mA/cm²)	L (cd/m²)	EQE (%)
2	0.001311851	0	0	5.1	27.3736	2283.647	9.77876
2.1	0.001678735	0	0	5.2	30.48898	2306.692	8.87898
2.2	0.002109931	0	0	5.3	35.19158	2388.968	7.95828
2.3	0.003524325	0	0	5.4	38.83413	2473.188	7.4618
2.4	0.00649945	0	0	5.5	42.4707	2549.919	7.03249
2.5	0.012107795	0	0	5.6	47.48045	2599.039	6.40746
2.6	0.02380793	0	0	5.7	52.2126	2642.167	5.92018
2.7	0.0379258	0	0	5.8	58.26258	2673.242	5.36515
2.8	0.062720525	0	0	5.9	63.31188	2700.889	4.98988
2.9	0.1061314	0	0	6	70.21393	2709.972	4.51289
3	0.1559186	0	10.03851	6.1	76.26465	2718.31	4.16607
3.1	0.234020875	8.28392	24.3939	6.2	81.0806	2719.027	3.92138
3.2	0.359319	65.39856	34.30875	6.3	88.93873	2699.48	3.54693
3.3	0.492496	109.44491	35.27826	6.4	93.81353	2684.249	3.34357
3.4	0.689216	180.14699	36.96412	6.5	101.4164	2647.054	3.04947
3.5	0.94605225	259.52477	36.5774	6.6	107.361	2547.041	2.77121
3.6	1.2743155	353.36322	35.68569	6.7	114.4623	2502.956	2.55359
3.7	1.684993	464.66822	34.44111	6.8	122.2889	2451.355	2.34292
3.8	2.1958195	583.71465	32.69204	6.9	128.9307	2406.611	2.178
3.9	4.5818775	731.90179	19.39201	7	136.3706	2324.634	1.99014
4	4.6323025	814.62524	21.23361	7.1	148.1038	2194.92	1.73169
4.1	5.57268	977.24591	21.00462	7.2	154.1344	2126.672	1.61106
4.2	5.385745	1111.0836	24.59661	7.3	163.5209	2008.16	1.43454
4.3	6.5471475	1266.50112	22.97478	7.4	171.9134	1925.228	1.30814
4.4	7.882355	1416.30831	21.28522	7.5	181.2265	1797.796	1.1581
4.5	9.4045475	1560.49491	19.5934	7.6	191.6984	1688.64	1.02812
4.6	12.2144275	1693.91322	16.36698	7.7	203.9819	1597.164	0.91258
4.7	14.6047175	1835.61997	14.80367	7.8	213.7275	1478.895	0.80571
4.8	17.7617475	1962.05174	12.98863	7.9	224.1594	1362.239	0.7076
4.9	20.5009175	2080.6981	11.93142	8	236.6321	1252.693	0.6153
5	23.2277675	2193.09963	11.07465				

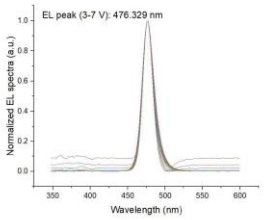
浙江中协立德质量检测技术有限公司
Zhejiang Zhongxie Lide Quality Testing Technology Co., Ltd.

№: WTS2026-A1093

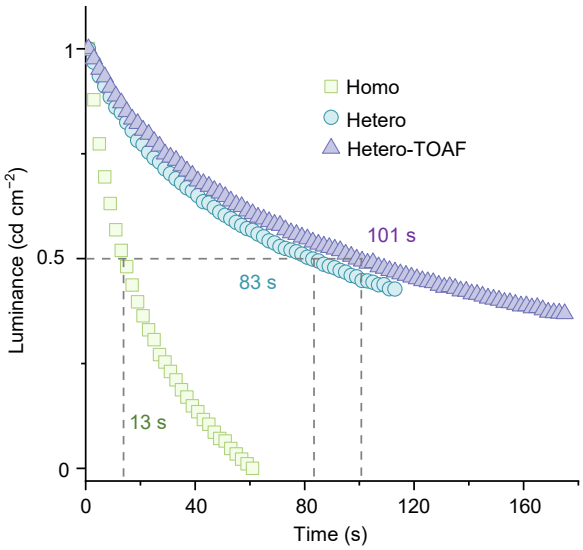
Attachment II



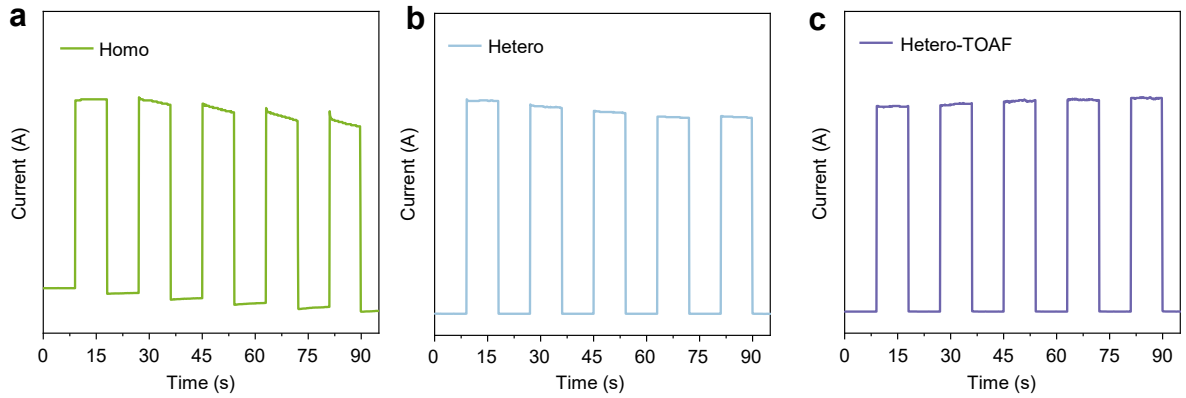
Attachment III



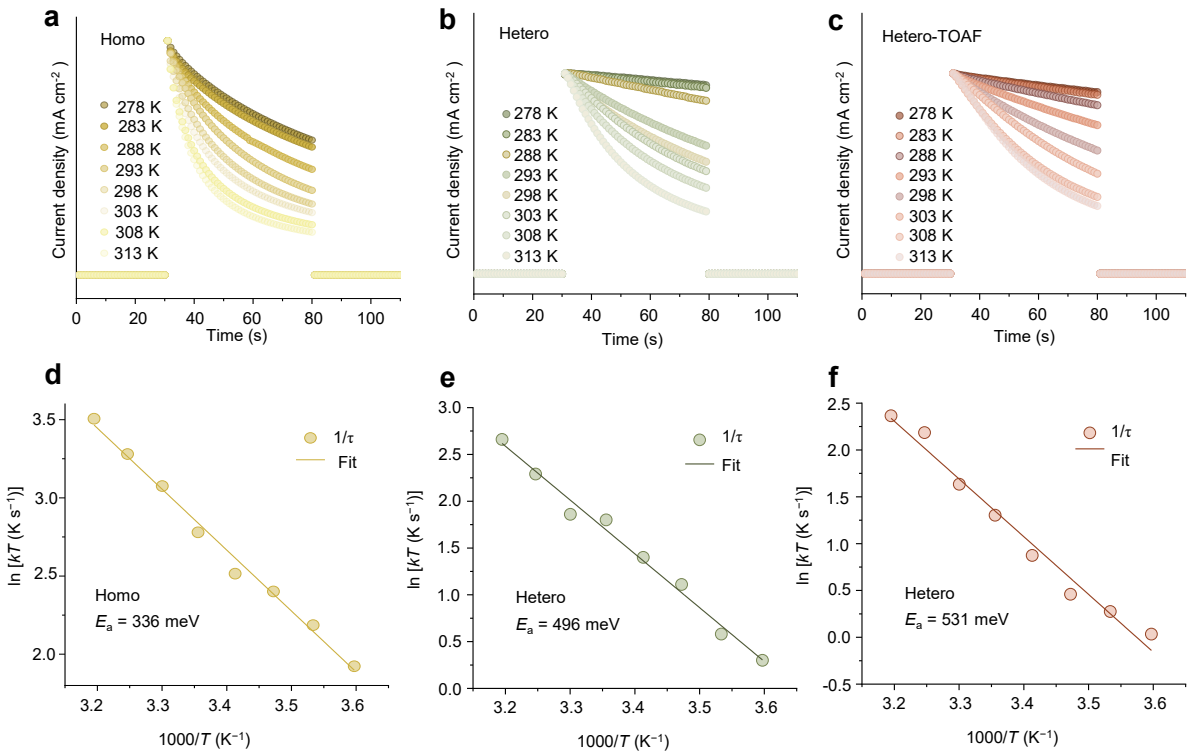
Supplementary Fig. 21. The third-party test report of the CsPbBrxCl3-x QD-based LEDs.



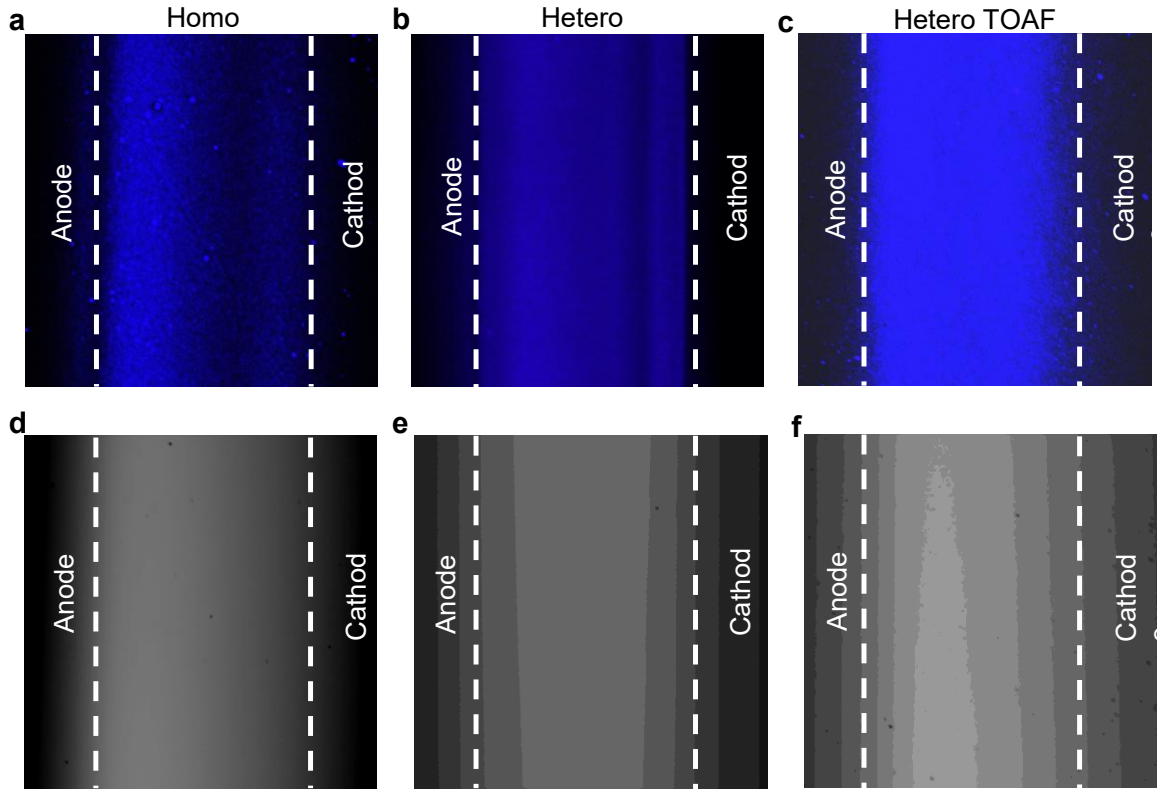
Supplementary Fig. 22. Operation stability. T_{50} measurements for the LEDs at an initial luminance of 100 cd m^{-2}



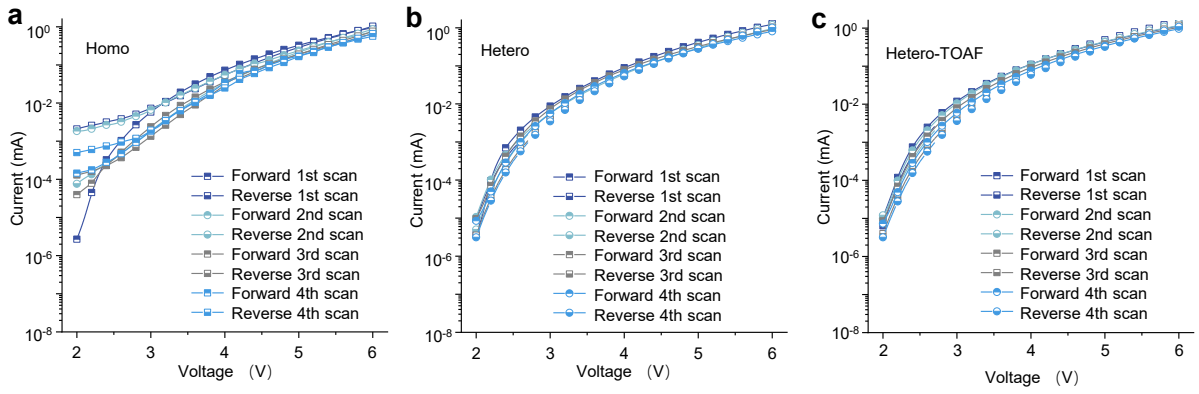
Supplementary Fig. 23. Transient photocurrent responses. a-c, Transient photocurrent responses of LEDs based on homo-QDs (**a**), hetero-QDs (**b**), and hetero-TOAF-QDs (**c**).



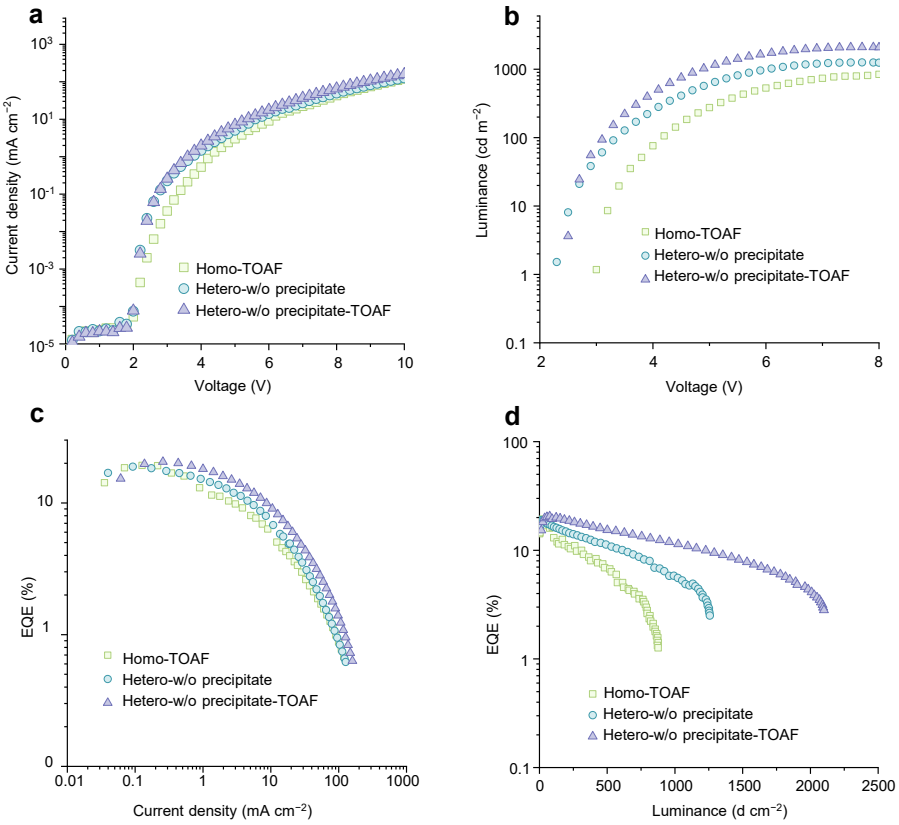
Supplementary Fig. 24. Determination of ion migration activation energy. a-c, Arrhenius plots of conductivity for devices based on homo-QDs (**a**), hetero-QDs (**b**) and hetero-TOAF-QDs (**c**) measured in the dark. **d-f**, Temperature-dependence plots of ln(kT) versus 1,000/T of homo-QDs (**d**), hetero-QDs (**e**), and hetero-TOAF-QDs (**f**). Solid lines represent linear fits used to extract E_a.



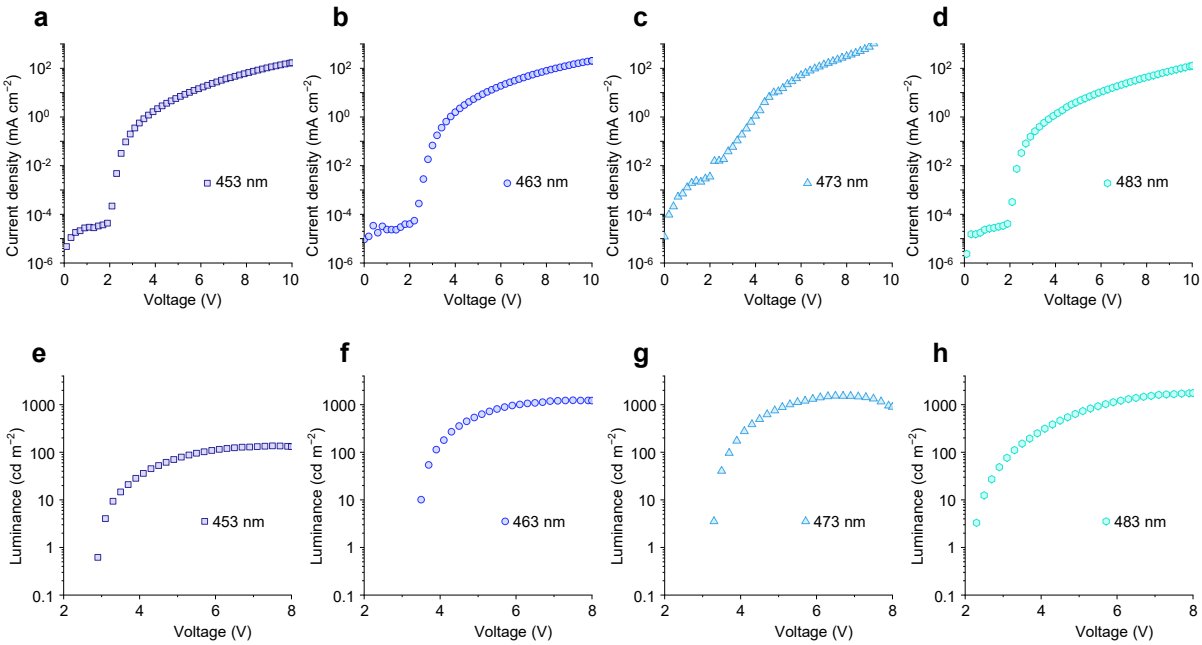
Supplementary Fig. 25. Ion migration. a-f, Fluorescence microscopy images of homo-QDs (**a** and **d**), hetero-QD (**b** and **e**), and hetero-TOAF-QD (**c** and **f**) films after poling at 2.0 V μm^{-1} for 4 h.



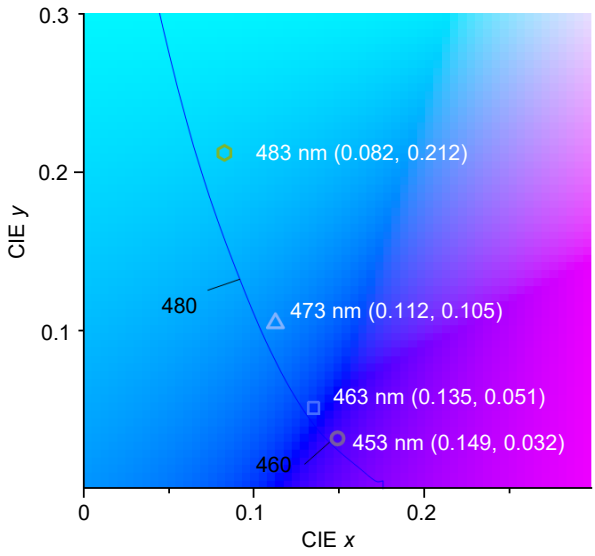
Supplementary Fig. 26. Stability characterization of LEDs. a-c, *I-V* curves of forward and reverse scans for LEDs based on homo-QDs (**a**), hetero-QDs (**b**), and hetero-TOAF-QDs (**c**).



Supplementary Fig. 27. Separating the effects of TOAF surface passivation and the heterogeneous synthesis strategy. a, Current density-voltage curves. **b**, Luminance-voltage curves. **c**, EQE as a function of current density. **d**, EQE as a function of luminance.



Supplementary Fig. 28. Electroluminescence performance of blue LEDs with different emission wavelengths. a-d, Current density-voltage curves of devices with peak emission at 453 nm (**a**), 463 nm (**b**), 473 nm (**c**), and 483 nm (**d**). **e-h**, Luminance-voltage curves of devices with peak emission at 453 nm (**e**), 463 nm (**f**), 473 nm (**g**), and 483 nm (**h**).



Supplementary Fig. 29. Colour purity of the tunable blue LEDs. Chromaticity coordinates of the devices presented in **Fig. 4**, plotted on the CIE 1931 colour space diagram.

Supplementary Table 1. Precursor feeding amounts for the synthesis of QDs with tunable PL peaks.

QDs	Cs (mmol)	FA (mmol)	Rb (mmol)	$PbCl_2$ (mmol)	$PbBr_2$ (mmol)	TOAB (mmol)	DDAC (mmol)
Homo-447 nm	0.0918	0.0081	0.0046	0.32	0.18	0.72	0.30
Homo-457 nm				0.25	0.25	0.72	0.30
Homo-462 nm				0.20	0.30	0.72	0.30
Homo-465 nm				0.19	0.31	0.72	0.30
Homo-469 nm				0.18	0.32	0.72	0.30
Homo-478 nm				0.12	0.38	0.72	0.30
Homo-480 nm				0.10	0.40	0.72	0.30
Homo-487 nm				0.09	0.41	0.72	0.30
Hetero-447 nm	0.0918	0.0081	0.0046	0.35	0.20	0.30	0.30
Hetero-457 nm				0.31	0.24	0.30	0.30
Hetero-462 nm				0.27	0.28	0.30	0.30
Hetero-465 nm				0.24	0.31	0.30	0.30
Hetero-469 nm				0.19	0.36	0.30	0.30
Hetero-478 nm				0.17	0.38	0.30	0.30
Hetero-480 nm				0.15	0.40	0.30	0.30
Hetero-487 nm				0.12	0.43	0.30	0.30

Supplementary Table 2. Wavelength-dependent PLQYs of the different QDs.

QDs	PLQY at various wavelengths (%)							
	447 (nm)	457 (nm)	462 (nm)	465 (nm)	469 (nm)	478 (nm)	480 (nm)	487 (nm)
Homo-QDs	6	10	20	31	34	53	58	76
Hetero-QDs	12	19	30	44	59	79	88	96
TOAF-QDs	16	38	62	72	88	96	99	99

Supplementary Table 3. Summarized device data of recently reported blue perovskite LEDs.

Perovskite	EL Peak (nm)	EQE (%)	Ref.
$CsPbBr_xCl_{3-x}$ QDs	448	3.4	1
$CsPbBr_xCl_{3-x}$ QDs	451	1.3	2
$CsPbBr_xCl_{3-x}$ QDs	460	12.0	3
$CsPbBr_xCl_{3-x}$ QDs	462	14.1	1
$CsPbBr_2Cl$ films	463	16.8	4
$CsPbBr_xCl_{3-x}$ films	465	10.6	5
$CsPbBr_xCl_{3-x}$ QDs	465	11.0	6
$CsPbBr_xCl_{3-x}$ QDs	465	16.7	3
$CsPbBr_xCl_{3-x}$ QDs	467	14.8	7
$CsPbBr_2Cl$ films	468	22.0	4
$CsPbBr_xCl_{3-x}$ QDs	470	21.3	3
$CsPbBr_xCl_{3-x}$ QDs	470	22.7	1
$CsPbBr_xCl_{3-x}$ QDs	470	24.9	8
$CsPbBr_3$ QDs	472	20.0	9
$CsPbBr_xCl_{3-x}$ films	472	3.1	10
$CsPbBr_xCl_{3-x}$ films	473	14.0	11
$CsPbBr_xCl_{3-x}$ QDs	473	22.7	12
$CsPbBr_xCl_{3-x}$ QDs	474	23.4	1
$CsPbBr_xCl_{3-x}$ QDs	475	24.3	3
$CsPbBr_xCl_{3-x}$ films	476	19.1	5
$CsPbBr_xCl_{3-x}$ QDs	478	25.0	1
$CsPbBr_xCl_{3-x}$ QDs	480	26.4	3
$CsPbBr_3$ QDs	480	23.5	13
$CsPbBr_xCl_{3-x}$ QDs	482	27.4	1
$CsPbBr_xCl_{3-x}$ films	483	24.6	5

$CsPbBr_xCl_{3-x}$ QDs	486	28.7	14
$CsPbBr_xCl_{3-x}$ films	488	23.8	11
$CsPbBr_xCl_{3-x}$ QDs	488	5.75	15
$CsPbBr_xCl_{3-x}$ QDs	490	23.5	16
$CsPbBr_3$ QDs	492	13.6	17
$CsPbBr_xCl_{3-x}$ films	495	21.5	18
$PEA_2Cs_{n-1}Pb_n(Cl_xBr_{1-x})_{3n+1}$ films	496	21.8	19
$CsPbBr_xCl_{3-x}$ QDs	453	6.13	This work
$CsPbBr_xCl_{3-x}$ QDs	457	14.16	This work
$CsPbBr_xCl_{3-x}$ QDs	463	25.50	This work
$CsPbBr_xCl_{3-x}$ QDs	473	36.39	This work
$CsPbBr_xCl_{3-x}$ QDs	476	36.92	This work
$CsPbBr_xCl_{3-x}$ QDs	483	35.48	This work

References and Notes

1 Cao, Q. *et al.* Surface-ligand-triggered synthetic control of defects in nanocrystals toward high-efficiency blue electroluminescence. *The Innovation* **7**, 101273 (2026).

2 Hong, Y. *et al.* Perovskite nanocrystals protected by hermetically sealing for highly bright and stable deep-blue light-emitting diodes. *Adv. Sci.* **10**, 2302906 (2023).

3 Gao, Y. *et al.* Highly efficient blue light-emitting diodes based on mixed-halide perovskites with reduced chlorine defects. *Sci. Adv.* **10**, eado5645 (2024).

4 Wang, Y. *et al.* Isomeric multi-hydrogen-bonding enables blue perovskite LEDs. *Nature* **655**, 617–623 (2026).

5 Mao, J. *et al.* Interface-regulated vapour crystallization for ultrapure perovskite LEDs. *Nat. Synth.* **5**, 1712–1723 (2026).

6 Li, J. *et al.* Efficient deep-blue (465 nm) perovskite quantum dot-based light-emitting diodes via triphenylamine derivative tailored hole transport engineering. *Adv. Funct. Mater.* **35**, 2412367 (2025).

7 Maimaitizi, H., Ågren, H. & Chen, G. Multifunctional ligand engineering enables high-performance $CsPb(Br/Cl)_3$ nanocrystals toward efficient and stable pure-blue perovskite LEDs. *Light Sci. Appl.* **15**, 135 (2026).

8 Nong, Y., Yao, J. & Song, J. Cation-anion-pair-assisted synthesis strategy enables high-performance pure blue perovskite quantum dot-based light-emitting diodes. *Adv. Funct. Mater.* **36**, e20569 (2026).

9 Xie, M. *et al.* Ultra-low efficiency roll-off high color purity blue perovskite quantum dot LEDs with exceeding 20% efficiency. *Light Sci. Appl.* **15**, 176 (2026).

10 Kwon, J. *et al.* In situ molecular passivation for improved performance and spectral stability in thermally evaporated pure blue perovskite light-emitting diodes. *Ind. Chem. Mater.* **4**, 355–365 (2026).

11 Chen, H. *et al.* High-quality perovskite crystal for efficient and bright pure-blue light-emitting diodes with narrow emission. *Nat. Commun.* **17**, 4697 (2026).

12 Ma, Z. *et al.* Steric hindrance of ligands inhibits interface ion penetration in perovskite nanocrystal-based electroluminescence devices. *ACS Energy Lett.* **10**, 5754–5761 (2025).

13 Cao, Q. *et al.* Isotropic-grown ultrasmall $CsPbBr_3$ nanocrystals in an enlarged synthesis toward efficient blue electroluminescence. *ACS Nano* **19**, 42455–42465 (2025).

14 Nong, Y. *et al.* The inserted dipole layer enables highly powerful blue perovskite quantum dot-based light-emitting diodes. *Sci. Bull.* **71**, 2758–2766 (2026).

15 Wu, X. *et al.* Ligand-mediated intergrain isolation strategy for narrow-emission deep-blue perovskite quantum dot light-emitting diodes. *ACS Photonics* **13**, 1537–1545 (2026).

16 Nong, Y. *et al.* Boosting external quantum efficiency of blue perovskite QLEDs exceeding 23% by trifluoroacetate passivation and mixed hole transportation design. *Adv. Mater.* **36**, 2402325 (2024).

17 Zhu, M. *et al.* Highly efficient sky-blue perovskite quantum dot light-emitting diodes via ligand-assisted trap-state passivation. *Energy Environ. Mater.* **9**, e70216 (2026).

18 Zheng, S. *et al.* Stable sky-blue perovskite LEDs achieved by efficient sub-bandgap emission with 24.5% PCE. *Adv. Funct. Mater.* **36**, e21079 (2026).

19 Zhang, L. *et al.* Photovoltage-driven two-transistor-one-diode perovskite pixels for in-cell optical sensing displays. *Adv. Mater.* **38**, e22776 (2026).